Magnetically Actuated Dynamic Iridescence Inspired by the Neon Tetra

*Zhiren Luo,[1] Benjamin Aaron Evans,[2] and Chih-Hao Chang[1,]**

[1]Department of Mechanical and Aerospace Engineering, North Carolina State University

Raleigh, NC 27695, USA

[2]Department of Physics, Elon University, Elon, NC 27244, USA

*Corresponding author: chichang@ncsu.edu

Supplementary Section A: Synthesis and Characterization of FFPDMS

Synthesis of FFPDMS

All details regarding synthesis of the FFPDMS material have been previously reported[53]. The iron oxide nanoparticles (7-10 nm) are precipitated from ferric chloride and ferrous chloride salts with 2:1 molar concentration in ammonium hydroxide solution. After precipitation, the nanoparticle aqueous solution is mixed with a copolymer of aminopropylmethylsiloxane (APMS) and dimethyllsiloxane (DMS) with 6-7 mol% APMS, and then stirred vigorously for 24 hours (pH 6.8 - 10). The amine groups on siloxane copolymer will adsorb onto the surface of positively-charged iron oxide nanoparticles to yield a siloxane-magnetite complex, which results in a black sediment in the solution. Then sediment is then rinsed in methanol, water, and methanol again (5 times for each rinse step) with sedimentation facilitated by a permanent magnet. The complex can be diluted by suspending it and APMS-co-DMS copolymer in chloroform, ultra-sonicating for 30 seconds, and removing the chloroform solvent.

Characterization of FFPDMS

The uniformity and sizes (7 - 10 nm) of iron oxide nanoparticles in FFPDMS have been verified by SEM and TEM measurement previously[53]. The magnetic properties of FFPDMS with different concentrations have also been measured using superconducting quantum interference device (SQUID) magnetometry [53] and no significant hysteresis was observed, indicating it is superparamagnetic. Since magnetization increases linearly with nanoparticle concentration in this material,[53] a linear interpolation indicates that the magnetization of 25 wt% magnetite nanoparticles at 300 mT is 8.68 Am^2/kg and the saturation magnetization at 5 T is 12.98 Am^2/kg. The magnetization curve of FFPDMS (25 wt% magnetite) is extracted from previous work and plotted in Supplementary Fig. S1a and verified by experimental measurement, shown in

Supplementary Fig. S1b. Also, this magnetization curve will be utilized as the input material properties in the magnetic finite element modeling of FFPDMS template, whose result is shown in Fig. 4c. Note that the iron oxide nanoparticles in FFPDMS have diameter of about 10 nm and are superparamagnetic, which is also verified by the small coercivity in the magnetic measurement. The coercivity of FFPDMS is estimated to be 31 Oe, namely a field of 0.0031 T is required to return the magnetization to zero, as shown in the insert of Supplementary Fig. S1b

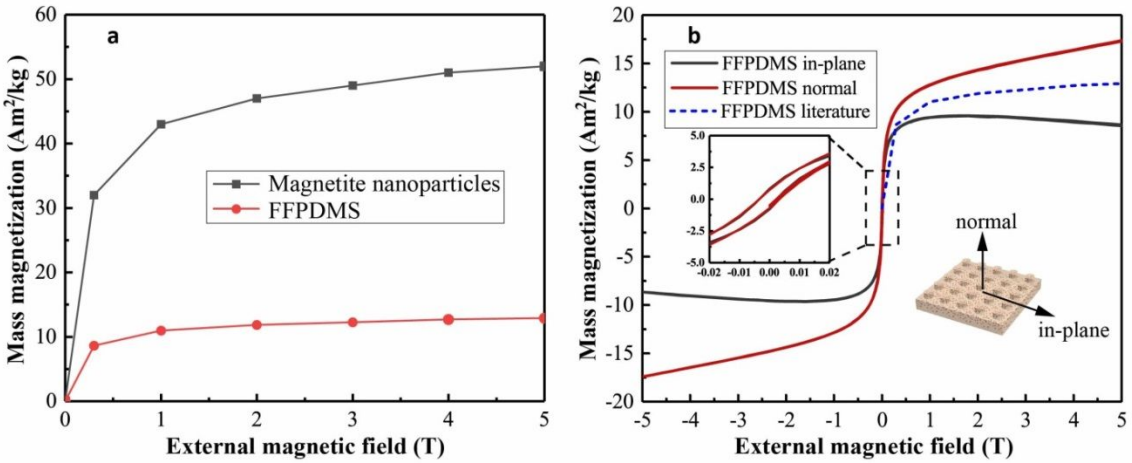

Supplementary Fig S1. The magnetic properties of FFPDMS. **a** The mass magnetization of the magnetite nanoparticles and FFPDMS with 25 wt% iron oxide nanoparticles which are extracted from literature. **b** The experimental measurement of mass magnetization for FFPDMS.

Supplementary Section B: Interference lithography and soft lithography

The patterning of the magnetic template is achieved using laser interference lithography (IL) and soft lithography. First, an ARC (i-CON-7, Brewer Science) film with 91 nm thickness is spun onto silicon wafer and baked at 185℃ for 1 minute on a hotplate to reduce back reflection. A negative photoresist SU-8 (2002 and 2000 thinner, Microchem) is then spincoated with 1 μm thickness and soft baked at 95℃ for 1 minute on a hotplate. A sample with about 8 mm by 8 mm size was cleaved for exposure. After two separated orthogonal laser ($\lambda = 325$ nm) exposures using Lloyd's mirror IL (incident angle = 4.66°, each exposure dose = 4.5 $\mathrm{mJ/cm^2}$), a square hole array with 2 μm period was patterned in the SU-8 film. The film was post-exposure baked at 90℃ for 3 minutes on a hotplate, developed in propylene glycol monomethyl ether actate (PGMEA, Sigma Aldrich) for 1 minute, and rinsed with IPA (2-propanol, J.T Baker) for several seconds.

Using the SU-8 mold, 4 μL FFPDMS precursor with 25 wt% of iron oxide nanoparticles was applied by pipette, and kept in -29 inHg vacuum for 5 minutes to reduce air bubbles. Most part of residual FFPDMS outside the mold was removed gently by glass stick, then the sample was spun with 2000 rpm speed for 2 min to flatten the surface. Then the sample and a vial of 15 μL formaldehyde (37 wt% in water, Fisher Chemical) were put separately into the desiccator and kept in -29 inHg vacuum for 6 hours. The FFPMDS would be crosslinked by the vapor deposition of formaldehyde.

After FFPDMS was cured, the sample was treated by oxygen plasma for 2 minutes. To transfer the surface, PDMS (Sylgard 184, Dow Corning, mixing ratio = 10:1) was applied on the surface of solid FFPDMS and kept in -29 inHg vacuum for 5 minutes to remove bubbles. Then the whole sample was spun with 500 rpm speed for 2 minutes. Afterward, a piece of silicon wafer was

treated by oxygen plasma for 2 minutes, and attached faced-down on the PDMS sample to form a sandwich-like integration. The integration was kept in -29 inHg vacuum for 5 minutes to remove bubbles, and heated on hotplate with 100℃ for one hour to cure the PDMS. Finally, the FFPDMS template was mechanically separated from SU-8 mold by a blade. As a result, the final sample is the FFPDMS template bonded on silicon substrate by PDMS.

Supplementary Section C: Characterization of Ferrofluid

In this paper, a 2 vol% water-based ferrofluid (EMG 707, FerroTec) is diluted by deionized water with ratio of 1:16, therefore the nanoparticle concentration is 0.125 vol%. The transmission electron microscope (TEM) image and corresponding element analysis have been done for the iron oxide nanoparticles in ferrofluid using Talos F200X, as shown in Supplementary Fig. S2. The diameter of thirty individual particles are extracted and measured from Supplementary Fig. S2a, yielding an average diameter of 11.5 nm with standard deviation of 3.3 nm, which matches with the data specification from the company (nominal diameter 10 nm). In addition, the element analysis verifies that the observed particles are iron oxide, shown in Supplementary Fig. S2b.

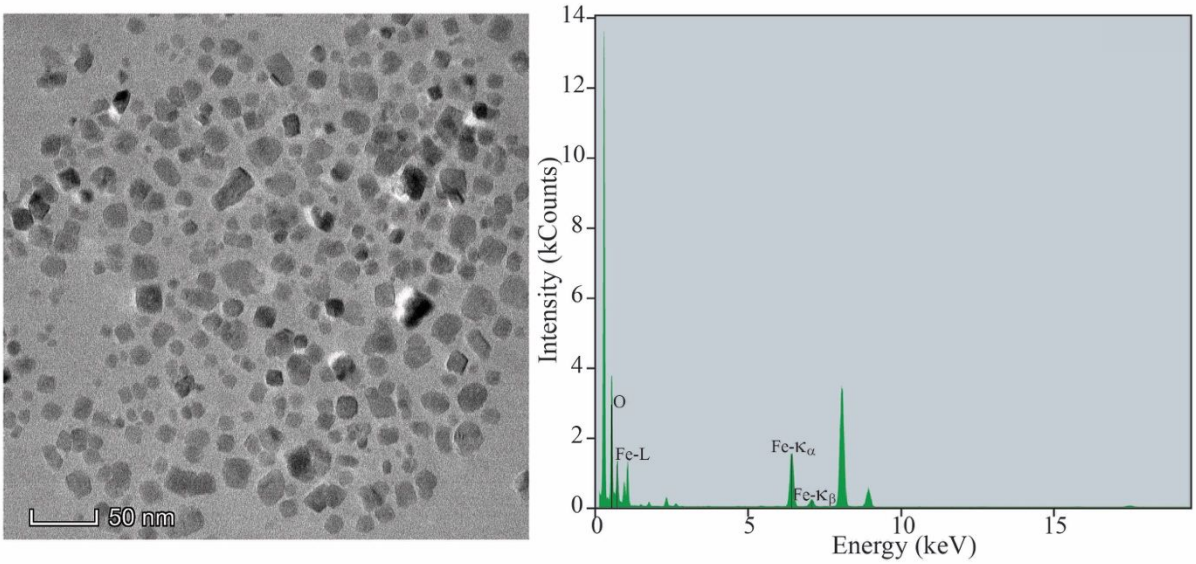

Supplementary Fig S2. Characterization of the iron oxide nanoparticles in Ferrofluid. **a** TEM image of iron oxide nanoparticles. The scale bar is 50 nm. **b** The element analysis of TEM image verifies that the observed particles are iron oxide.

Supplementary Section D: Response Time of Self-Assembled Columns

The response time of the self-assembly columns (SACs) disassembly on the FFPDMS magnetic template array has been characterized by analyzing the extracted images from microscopy videos, as displayed in Supplementary Fig. S3. In the sequence of images extracted from a movie, the out-of-plane external field is removed at time $t = 0$ s. Afterward the SACs collapse, and the iron oxide nanoparticles disperse uniformly into the water, resulting in the blurred image of the low-aspect-ratio of the FFPDMS template. The transition is completed within 0.3 s. The assembly and tilting of the SACs occur in shorter amount of time, resulting in less than 0.1 s lag between magnetization and actuation.

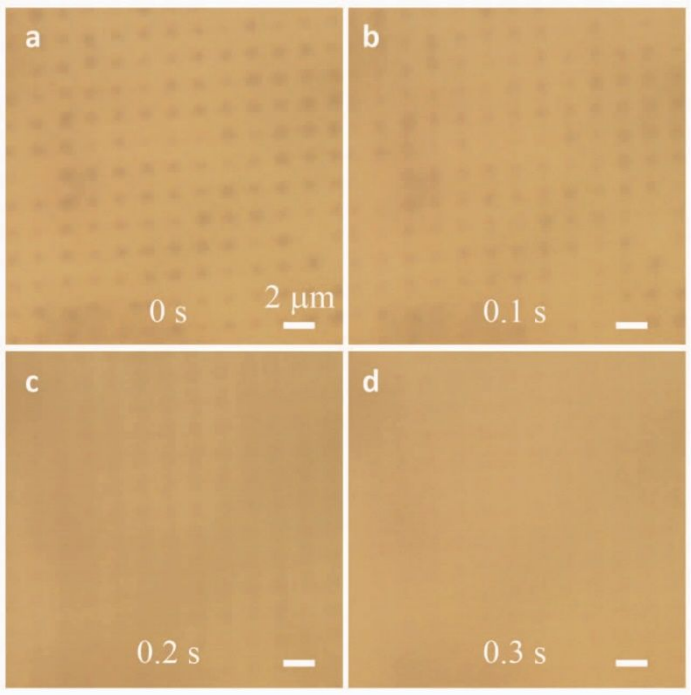

Supplementary Fig S3. Top-view microscopy images of the disassembly process when the external field is removed. The microscopy images are taken at **a** 0 s, **b** 0.1 s, **c** 0.2 s, **d** 0.3 s. The scale bars are 2 μm.

Supplementary Section E: The Magnetization and Magnetic Force of FFPDMS

This section describes the simulation of magnetic fields and forces generated when the FFPDMS template is magnetized, which lead to the assembly and anchoring of the SACs. The external field is applied by a cylindrical permanent magnet (FeNdB, J&K magnetics, diameter 25.4 mm, height 40 mm). The magnetic field distribution contour around the permanent magnet can be numerical calculated using software FEMM, which is shown in Supplementary Fig. S4. Here the field is along the z direction when centered on the axis of the cylindrical magnet, which is extracted from the contour and plotted in Supplementary Fig. S5a. The field decreases as z increases, and reaches 0.25 T at $z = 11.16$ mm, which is the distance to the substrate. Particularly, the field at the structure position (from $z = 11.16$ mm to $z = 11.18$ mm) is further extracted in Supplementary Fig. S5b. Since the structure is only around 20 μm thick along the z axis, the field gradient is only around 15 T/m. Therefore, the field from the permanent magnet can be regard as uniform when compared with the local field gradient induced by the magnetic template (4×10^4 T/m).

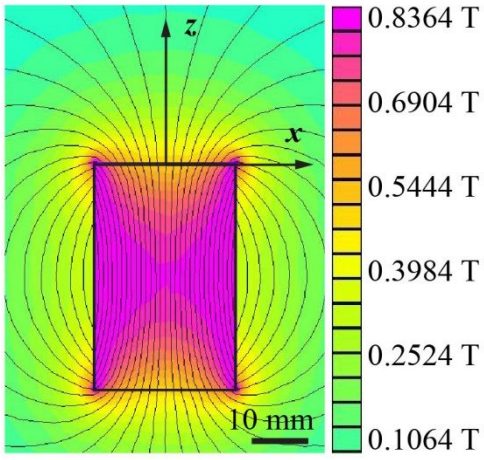

Supplementary Fig S4 The magnetic field distribution contour of the permanent magnet.

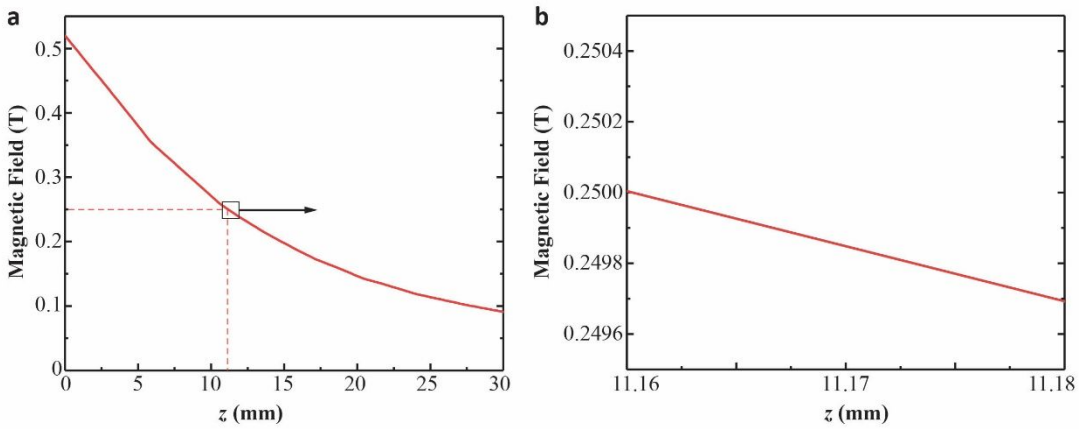

Supplementary Fig S5 The magnetic field along z axis above the permanent magnet. **a** The field from $z = 0$ mm to $z = 30$ mm. **b** The field from $z = 11.16$ mm to $z = 11.18$ mm, where the fabricated structure is located at.

When an external field of 0.25 T is applied in the out-of-plane direction, the FFPDMS template generates a periodic field distribution as shown in Fig. 4c. The generated magnetic force F on a single nanoparticle is given by:

$$F = \nabla(\boldsymbol{m} \cdot \boldsymbol{B}) = \rho V \nabla(\boldsymbol{M} \cdot \boldsymbol{B}) = \rho V \nabla(M_{\mathrm{x}} B_{\mathrm{x}} + M_{\mathrm{y}} B_{\mathrm{y}} + M_{\mathrm{z}} B_{\mathrm{z}})$$

Here, $\boldsymbol{m}$ is the magnetic moment vector which is given by $\boldsymbol{m} = \rho V \boldsymbol{M}$. The nanoparticles are approximated as spheres and the estimated volume is $V = \frac{4}{3}\pi \times \left(\frac{10\ \mathrm{nm}}{2}\right)^3 = 5.236 \times 10^{-25}\ \mathrm{m}^3$. The mass density is set as $\rho = 5000 \mathrm{kg/m}^3$. $\boldsymbol{M}$ and $\boldsymbol{B}$ are the vectors of magnetization and magnetic field, the latter including the external field from magnet plus the local field from template, and their dot product is described by components in x, y and z directions, such as M_{x} and B_{x}. Since $\boldsymbol{M}$ does not reach saturation magnetization at 0.25 T external field and is assumed uniformly distributed inside the single iron oxide nanoparticle, $\boldsymbol{M}$ can be expressed as:

$$\boldsymbol{M} = \frac{1}{\mu_0} \chi \cdot \boldsymbol{B}$$

Here, μ_0 is vacuum magnetic permeability, and the mass susceptibility of iron oxide nanoparticle is $\chi = 1.341 \times 10^{-4} \mathrm{m}^3/\mathrm{kg}$, which is approximated as the slope of magnetization

curve in Supplementary Fig. S1 since the magnetization can be regarded as linear from zero to 0.25 T. As a result, the horizontal magnetic force F_{x} applied on iron oxide nanoparticles in ferrofluid can be calculated from the field gradient as:

$$F_{\mathrm{x}} = \rho V \frac{\partial}{\partial x}\left(\frac{1}{\mu_0}\chi \cdot \boldsymbol{B} \cdot \boldsymbol{B}\right) = 2 \cdot \frac{\chi}{\mu_0} \cdot \rho V \cdot \left(B_{\mathrm{x}}\frac{\partial B_{\mathrm{x}}}{\partial x} + B_{\mathrm{z}}\frac{\partial B_{\mathrm{z}}}{\partial x}\right)$$

The B_x and B_{z} are extracted from color map at $\varphi_{\mathrm{m}} = 0°$ in Fig. 4c to calculate field gradient component $\frac{\partial B_{\mathrm{x}}}{\partial x}$ and $\frac{\partial B_{\mathrm{z}}}{\partial x}$. Components in y direction are ignored in this 2D analysis. Finally, the horizontal magnetic forces F_{x} have been worked out and denoted in Supplementary Fig. S6a. When $z = 0$ μm, F_{x} reaches a peak value of $F_{\mathrm{peak}} = 5.28 \times 10^{-15}$ N near the edge of FFPDMS pillar at $x = \pm 0.5$ μm and points toward the center ($x = 0$ μm) where $F_0 = 0$ N. This force validates the "anchor" effect that pulls the particles towards the pillar center, shown as the red arrows in the figure. The force F_{x} decreases dramatically when z increases. For example, the peak force F_{x} drops down to 8.50×10^{-16} N at $z = 0.25$ μm, and becomes 1.03×10^{-16} N at $z = 1$ μm. It rapidly approaches zero as $z > 1$ μm, since the magnetic template generates little field gradient at such distance. This implies the "anchor" effect only exists around the bases of the SACs and will not affect the tilt actuation of the upper portions of the SACs.

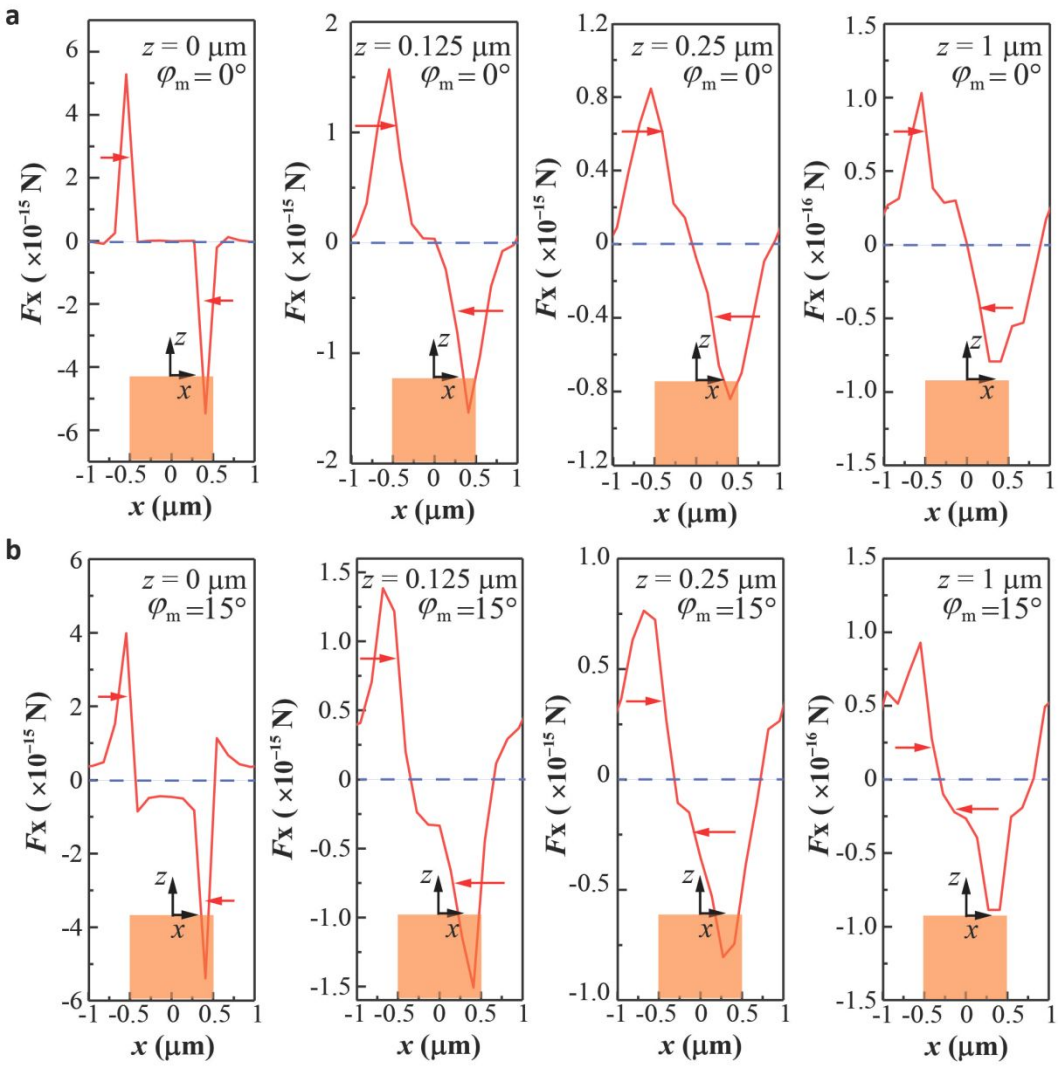

Supplementary Fig S6 The magnetic forces at $z = 0$ μm, $z = 0.125$ μm, $z = 0.25$ μm, $z = 1$ μm when **a** $\varphi_m = 0°$ and **b** $\varphi_m = 15°$, respectively.

Similarly, The curves of F_x verses x at $\varphi_m = 15°$ are calculated and displayed in Supplementary Fig. S6b. Here, the positions of peak force F_{peak} and equilibrium center with zero force F_0 all shift about 0.25 μm toward negative direction along x axis, corresponding to the direction of tilted external field. This indicates that when the external field is tilted, not only the upper parts of the SACs will tilt along the external field direction, but also the base of the SACs will shift slightly according to the external field.

Using this model, the peak forces F_{peak} verses z at different tilt angles are shown in Fig. 4d to describe the influence of tilt angle φ_{m}. It can be observed that the peak force F_{peak} decreases more and more rapidly as z increases in all cases. This also confirms the working range of "anchor" effect in Supplementary Fig. S6. In addition, when $z < 0.25$ μm, the F_{peak} decreases for higher φ_{m}. However, when $z > 0.25$ μm, all peak forces tend to be the same despite of different tilt angles. This is also confirmed by the experiments, where to top of the SACs are free to move for any φ_{m} for effective tilt actuation.

To examine the "anchor effect" in comparison with random motion induced by thermodynamics, the effective force of thermal fluctuation can be simply approximated as the division of the energy by the displacement:

$$F_{\text{th}} = \frac{\frac{1}{2}k_{\text{B}}T}{\Delta x}$$

Here, $\frac{1}{2}k_{\text{B}}T$ is the energy in the Brownian motion based on equipartition theorem, and Δx is assumed as the potential displacement of the nanoparticle in the trap, which is assumed as the diameter of the FFPDMS pillar, namely $\Delta x = 1$μm. k_{B} is the Boltzmann constant, and T is set as the room temperature (293 K). The effective thermal fluctuation force F_{th} is shown as the straight line in Fig. 4d. It indicates that when $\varphi_{\text{m}} \leq 30°$ and $z < 0.125$ μm, the peak magnetic force F_{peak} can overcome the force F_{th}, which is consistent with experimental observations. However, at higher z away from the template $F_{\text{peak}} < F_{\text{th}}$, therefore random fluctuation of the SAC top is expected.

Supplementary Section F: Field-Induced Nanoparticle Assembly on Non-Magnetic Templates

In the previous section the critical role of the magnetic FFPDMS template is described, which generates a periodic field profile that contributing to the anchoring forces. This section describes the assembly results when a non-magnetic PDMS periodic template was applied to guide field-induced aggregation. The goal is to verify the prediction that the SAC formation is possible on a non-magnetic template, as illustrated in Supplementary Fig S7 and Supplementary Movie. S2. While the particle assembles are guided by the PDMS template under an out-of-plane magnetic field, the SACs move around due to thermal fluctuations. Therefore, the particle assembly can be observed to be stable but not "anchored." When the magnetic field is tilted, the SACs slide from the top of one pillar to another instead of tilting and are no longer perfectly periodic. This can be attributed to the fact that the PDMS nanopillars do not generate a periodic magnetic field profile near the surface. Due to a lack of field gradient, there is no horizontal force to anchor the assembly of the nanoparticles, as discussed in Supplementary Section E. This demonstrates the importance of "anchor" effect, without which the SACs lack long-range order, fluctuate in the liquid environment, and cannot be tilted by changing the magnetic field. In comparison, the SACs on FFPDMS templates are anchored down to the top of the pillars with rotation about the base as the only degree of freedom.

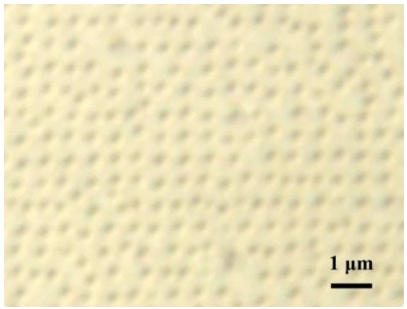

Supplementary Fig S7 The SACs on PDMS pillar array under out-of-plane magnetic field.

Supplementary Section G: The Dynamic Tilt Range of SACs

The tilt range of SACs for magnetic actuation is estimated to be $\varphi_m \in [-30°, +30°]$, since larger field tilt angle result in column collapse and extend chain assembly across multiple template pillars. Experimental observation of the collapses of the SACs are depicted in the top-view microscope images shown in Supplementary Fig. S8. As the external field angle is increased from 0° to 60°, the SACs remain aligned but start to degrade when $\varphi_m = 35°$ while most of them collapse or disperse into fluid when $\varphi_m = 60°$, as noted by the white dash ellipses. The remaining SACs tend to form long chains with non-uniformity diameter, evidence of energy imbalance between magnetic and surface energies. The tilted SACs also continuously slide toward the magnet direction. This is attributed to the horizontal shear magnetic forces and field gradient and low anchoring forces at large field angles. As a result, the SACs are not periodic and the quality is too low to result in tunable optical properties at large tilt angles. Evidence of some assembly degradation initiates at φ_m~30°, leading towards the estimate operation range. This result also confirms the simulation results in Fig. 4c and 4d.

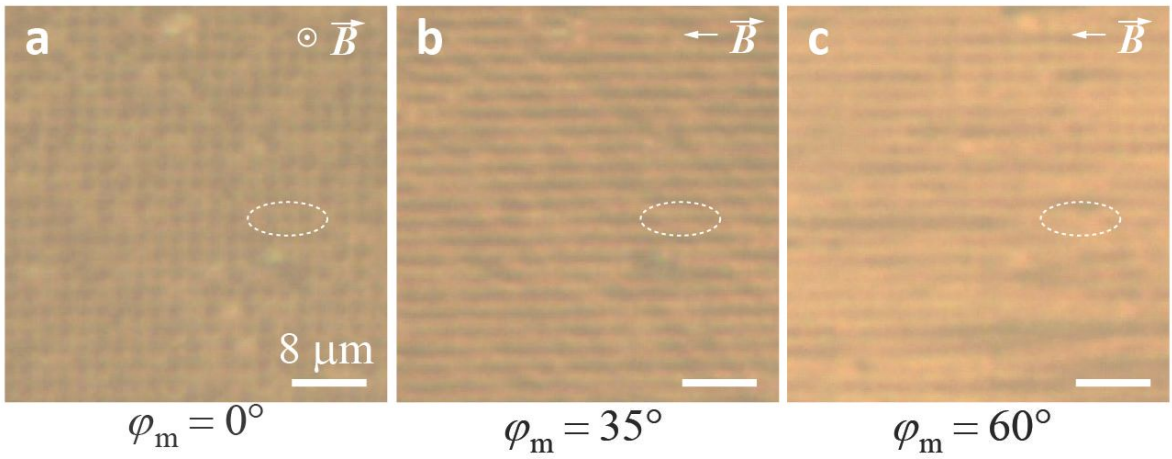

Supplementary Fig S8. Degradation of SACs at large tilt angles. **a** The SACs stand vertically and are stable when $\varphi_m = 0°$. **b** The SACs start to degrade when $\varphi_m = 35°$. **c** Most of SACs collapse when $\varphi_m = 60°$. The scale bars in all three images are 8 μm. The white dash ellipses show the degradation process of three SACs.

Supplementary Section H: Optical Characterization of Dynamic Iridescent Sample

When a periodic structure is illuminated, the light is diffracted into discrete orders dependent on the structure period and incident wavelength. This can create iridescent effects, where the changes in reflectance spectra at different viewing angles lead to different observed colors. This section describes the operating principle and characterization details for the dynamic color change. For a periodic diffraction grating with period of Λ, the reflection angle θ_m of m^{th} diffraction order is given by:

$$\Lambda \cdot (\sin\theta_m - \sin\theta_{\text{in}}) = m \cdot \lambda$$

Here, the period is $\Lambda = 2\ \mu\text{m}$ and wavelength is $\lambda = 633\ \text{nm}$. The reflection angle θ_m and the incident angle θ_{in} are both positive, namely they are located at different sides of normal axis. Therefore, the reflection angles of the $+1^{\text{st}}$, -1^{st}, and 0^{th} orders can be described respectively as:

$$\theta_{+1} = \arcsin\left(\frac{633\ \text{nm}}{2\ \mu\text{m}} + \sin\theta_{\text{in}}\right)$$

$$\theta_{-1} = \arcsin\left(\frac{(-1)\times 633\ \text{nm}}{2\ \mu\text{m}} + \sin\theta_{\text{in}}\right)$$

$$\theta_0 = \theta_{\text{in}}$$

When $\theta_{\text{in}} = 43°$ which serves as the critical angle, the θ_{+1} is close to 90°. Hence there is no $+1^{\text{st}}$ order when the incident angle goes beyond 43°. The ranges of angles for the reflection orders in the operation range are shown in Supplementary Fig. S9, which show excellent agreement between the optical model and experimental characterization.

The reflection efficiency contours of the $+1^{\text{st}}$ and 0^{th} orders for $\theta_{\text{in}} = 16°$ are displayed in Supplementary Fig. S10. Similar to the trend of the -1^{st} order, the peak reflection efficiency of the $+1^{\text{st}}$ order shows a symmetric trend with respect to the line $\varphi_{\text{m}} = 0°$. The diffraction-

independent 0^{th} order does not have peak efficiency trend, but has minimum efficiency instead when the incident angle is around 20° to 30°.

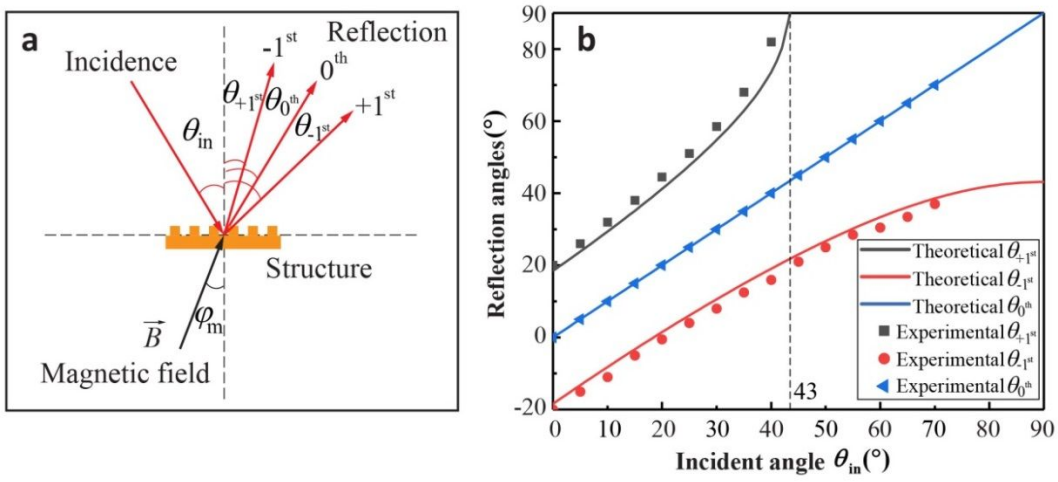

Supplementary Fig S9. The relationship between incident angle and reflection angle for the $+1^{st}$, -1^{st}, and 0^{th} orders. **a** The schematic of incidence and reflection orders. **b** The plot of incident angles and reflection angles. The solid lines are from theoretical calculations and the dots are from experimental measurements.

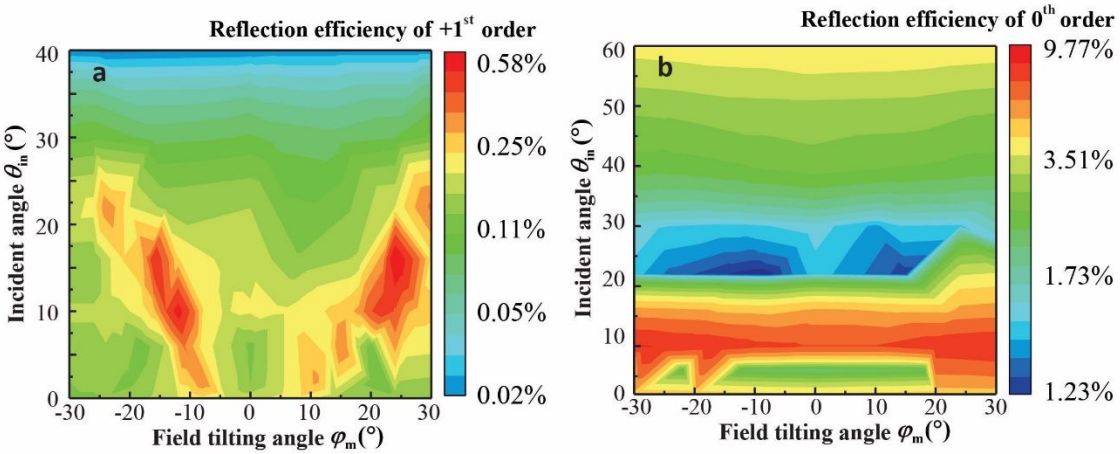

Supplementary Fig S10. The 2D contour of reflection efficiency for **a** the $+1^{st}$ order, and **b** the 0^{th} order with different incident angles.

To quantify the iridescence effect and structural color appearance, the reflectance spectra of different diffraction orders with various incident and viewing angles can be characterized using the optical setup shown in Supplementary Fig. S11a and S11c. Since the light source and detector are fixed and aligned along a single optical axis in the spectrophotometer, mirrors

(PF10-03-P01, Thorlabs) are applied to alter the light path for different reflected diffraction angles. In addition, the extra optical system increases the optical path length, shifting the position of the waist radius of the Gaussian beam. Therefore, a lens (LB 1471, Thorlabs) is utilized to guarantee that the position of waist radius is on the surface of the fabricated structure, and another lens (LB 1471, Thorlabs) is used to minimize the divergence of the light beam.

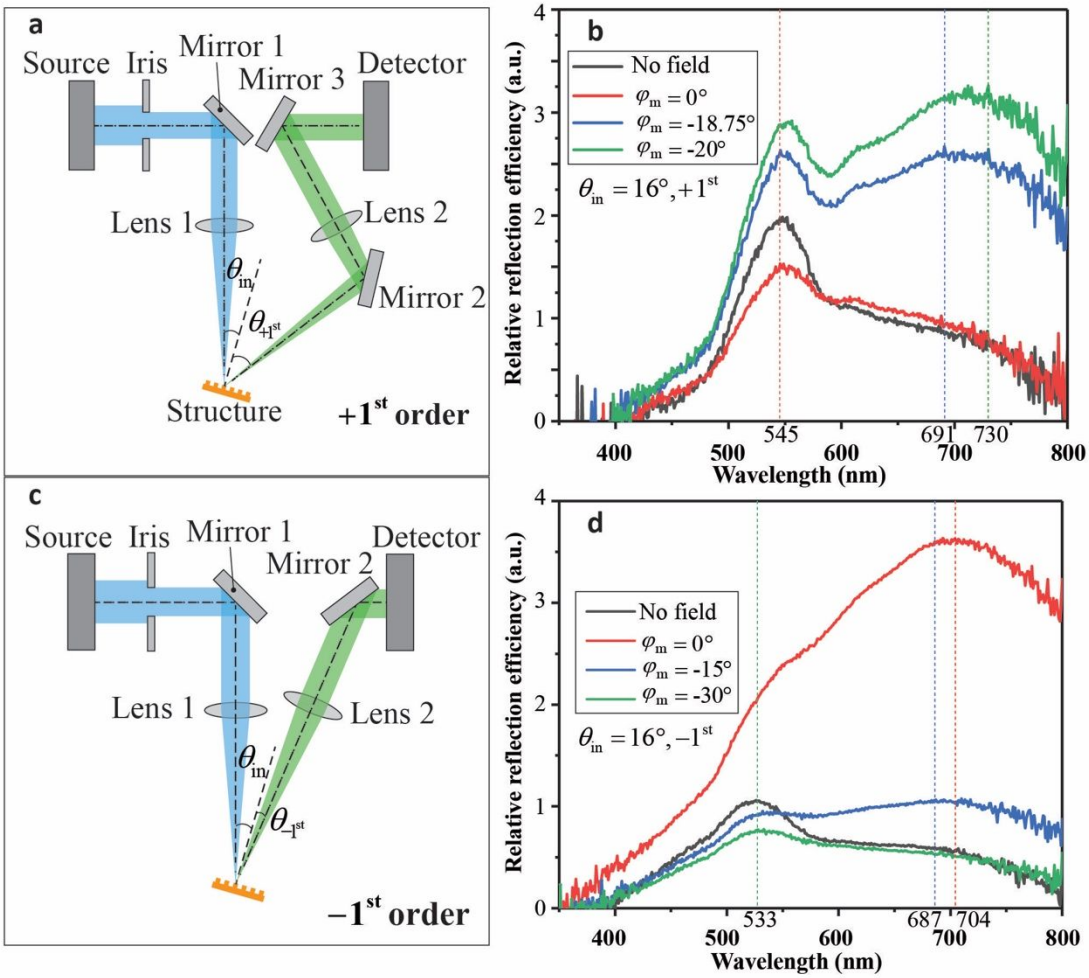

Supplementary Fig S11. The spectrometry measurement. **a** The schematic of the user-customized optical system inside the spectrometer chamber for the $+1^{st}$ order. **b** The spectra of the $+1^{st}$ order at $\theta_{in} = 16°$ with $\varphi_m < 0°$. **c** The schematic for the -1^{st} order. **d** The spectra of the -1^{st} order at $\theta_{in} = 16°$ with $\varphi_m < 0°$.

The dimensions of the experimental setup illustrated in Supplementary Fig. S11a are: $\theta_{in} = 16°$, $\theta_{+1^{st}} = 36.31°$, the distance between Lens 1 and the structure is 8.3 cm, the distance between

the structure and Mirror 2 is 8.5 cm, the distance between Mirror 2 and Lens 2 is 6 cm. The dimensions in Supplementary Fig. S11c are: $\theta_{\text{in}} = 16°$, $\theta_{-1^{\text{st}}} = -2.34°$ (the minus sign means $\theta_{-1^{\text{st}}}$ is at the same side as θ_{in}), the distance between Lens 1 and the structure is 8.3 cm, the distance between the structure and Lens 2 is 14.5 cm.

The measured reflectance spectra of the sample at incident angle of 16º and various magnetic field angle φ_{m} are shown in Fig. 6a and 6b in the main text. Here additional measured spectra of the $+1^{\text{st}}$ and -1^{st} orders with negative tilt angles $\varphi_{\text{m}} < 0°$ at $\theta_{\text{in}} = 16°$ are shown in Supplementary Fig. S11b and S11d. When the external field tilt angle changes from 0° to $-20°$, the peak wavelength of the $+1^{\text{st}}$ order increases from 545 nm to 730 nm with a red shift and a tunability of $\Delta\lambda/\lambda_0 = +33.9\%$. On the other hand, when the external magnetic field is tilted from 0° to $-30°$, the peak wavelength of the -1^{st} order experiences a blue shift from 704 nm to 533 nm with a tenability of $\Delta\lambda/\lambda_0 = -24.3\%$.

The shifts in the measured reflectance spectra can be modeled by using a simplified "Venetian blind" model. Since the actuated ferrofluid consists of SACs and water surrounding them, we assume iron oxide nanoparticles are closed-packed enough inside SACs with concentration of 65% by volume, the effective dielectric constant of the SACs ε_{SAC} can be approximated by Maxwell-Garnett Equation:

$$\varepsilon_{\text{SAC}} = \varepsilon_{\text{w}} \cdot \frac{[2\delta_{\text{m}}(\varepsilon_{\text{m}} - \varepsilon_{\text{w}}) + \varepsilon_{\text{m}} + 2\varepsilon_{\text{w}}]}{[2\varepsilon_{\text{w}} + \varepsilon_{\text{m}} + \delta_{\text{m}}(\varepsilon_{\text{w}} - \varepsilon_{\text{m}})]}$$

Here, ε_{w} is the dielectric constant of water, ε_{m} is the dielectric constant of magnetite nanoparticles, and the volume fraction of nanoparticles is $\delta_{\text{m}} = 0.65$. As the refractive index n can be expressed by dielectric constant (or relative permittivity) ε_{r} and relative permeability μ_{r}:

$$n = \sqrt{\varepsilon_r \mu_r} = \sqrt{\frac{\varepsilon\mu}{\varepsilon_0 \mu_0}}$$

Here, the ε and ε_0 are the permittivity of a specific medium and the vacuum permittivity, respectively; while μ and μ_0 are the permeability of a specific medium and the free space permeability, respectively. The refractive indices of iron oxide nanoparticle and water are $n_m = 2.34$ and $n_w = 1.33$, respectively, and the dielectric constants of iron oxide nanoparticle and water are $\varepsilon_m = 5.48$ and $\varepsilon_w = 1.77$, respectively (M. R. Querry. *Optical constants*, Contractor Report CRDC-CR-85034, 1985). Particularly, the relative permeability of iron oxide nanoparticle is close to 1 at visible frequencies, which can be verified by $\mu_m = n_m^2/\varepsilon_m$. Therefore, the refractive index of the SACs can be calculated as:

$$n_{SAC} = \sqrt{n_w^2 \cdot \frac{2\delta_m(n_m^2 - n_w^2) + n_m^2 + 2n_w^2}{n_m^2 + 2n_w^2 + \delta_m(n_w^2 - n_m^2)}}$$

Finally the $n_{SAC} = 1.92$ is obtained from the calculation.

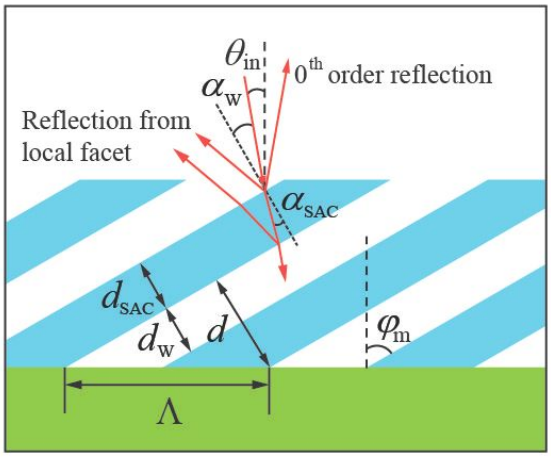

Supplementary Fig S12. The schematic of multilayer reflector. d_w and d_{SAC} are the thicknesses of the water layer and the SAC respectively along the facet normal of SACs. α_w and α_{SAC} are the refraction angles inside the water layer and the SAC respectively to the facet normal of SACs.

Based on a multilayer reflector which is illustrated in Supplementary Fig. S12, the peak wavelength λ is given by[4,12]:

$$\lambda = \frac{2}{m}(n_{\mathrm{w}} d_{\mathrm{w}} \cos(\alpha_{\mathrm{w}}) + n_{\mathrm{SAC}} d_{\mathrm{SAC}} \cos(\alpha_{\mathrm{SAC}}))$$

Here the m is the order of the multilayer reflector. d_{w} and d_{SAC} are the thicknesses of the water layer and the SAC, respectively, along the facet normal of SACs. Based on the concentration of the SACs, the thicknesses can be approximated to be the same, resulting in $d_{\mathrm{w}} = d_{\mathrm{SAC}} = \frac{1}{2}d = \frac{1}{2}\Lambda \cos(\varphi_{\mathrm{m}})$. α_{w} and $\alpha_{\mathrm{SAC}}$are the refraction angles inside the water layer and the SAC, respectively, defined relative to the facet normal of SACs. Assuming the incident light hits SAC first, then $\alpha_{\mathrm{w}} = 90° - \theta_{\mathrm{in}} - \varphi_{\mathrm{m}}$. Based on Snell's law, we have: $n_{\mathrm{w}} \sin(\alpha_{\mathrm{w}}) = n_{\mathrm{SAC}} \sin(\alpha_{\mathrm{SAC}})$. Therefore, the peak wavelength λ can be expressed in terms of the field tilt angle φ_{m}:

$$\lambda = \frac{2}{m}(d_{\mathrm{SAC}} \sqrt{n_{\mathrm{SAC}}^2 - n_{\mathrm{w}}^2 \sin^2(\alpha_{\mathrm{w}})} + d_{\mathrm{w}} n_{\mathrm{w}} \cos(\alpha_{\mathrm{w}}))$$

$$= \frac{1}{m}\Lambda \cos(\varphi_{\mathrm{m}})(\sqrt{n_{\mathrm{SAC}}^2 - n_{\mathrm{w}}^2 \cos^2(\theta_{\mathrm{in}} + \varphi_{\mathrm{m}})} + n_{\mathrm{w}} \sin(\theta_{\mathrm{in}} + \varphi_{\mathrm{m}}))$$

For incident angle $\theta_{\mathrm{in}} = 16°$, structure period $\Lambda = 2$ μm, and $m = 6$, the theoretical model can be calculated and compared with the measured spectrometry peak wavelength of the -1^{st} order, as shown in Fig. 6d.

Supplementary Movie 1. The actuation characterization of SACs on the FFPDMS pattern using optical microscopy. The SACs are actuated by an external magnetic field below the sample to tilt along *x* and *y* directions, and then rotate clockwise and counter-clockwise for several cycles. The SACs then collapse and disperse into water after the external field is removed.

Supplementary Movie 2. The actuation characterization of SACs on the PDMS pattern using optical microscopy. The SACs are guided by the square lattice of the template under a vertical external magnetic field, but tend to fluctuate and slides away when the external field is tilted.

Supplementary Movie 3. The dynamic iridescence demonstration of the reflected -1^{st} order at $\theta_{\mathrm{in}} = 16°$, which shows a blue shift. The movie consists of 3 quick cycles and 1 slow cycle. In each cycle, the field tilt angle φ_{m} changes from 0° to 30° and back to 0° again.

Supplementary Movie 4. The dynamic iridescence demonstration of the reflected $+1^{\mathrm{st}}$ order at $\theta_{\mathrm{in}} = 16°$, which shows a red shift. The movie consists of 3 quick cycles and a half slow cycle. In each cycle, the field tilt angle φ_{m} changes from 0° to 20° and back to 0° again. The tilt angle φ_{m} increases from 0° to 20° in last half slow cycle.

Supplementary Movie 5. The dynamic iridescence demonstration of the reflected -1^{st} order at $\theta_{\mathrm{in}} = 50°$, which shows a red shift. In this movie, the initiate color is green and it can shift to yellow. The movie consists of 4 quick cycles and a half slow cycle. In each cycle, the field tilt angle φ_{m} changes from 0° to 30° and back to 0° again. The tilt angle φ_{m} increases from 0° to 3 0° in last half slow cycle.

Supplementary Movie 6. The dynamic iridescence demonstration of the reflected -1^{st} order at $\theta_{\mathrm{in}} = 50°$ with different viewing angle, which shows a red shift. In this movie, the initiate color is close to indigo and it can shift to orange. The movie consists of 3 quick cycles and a half slow cycle. In each cycle, the field tilt angle φ_{m} changes from 0° to 30° and back to 0° again. In last half slow cycle, the tilt angle φ_{m} increases from 0° to 30°.

Supplementary Movie 7. The dynamic iridescence demonstration of the reflected -2^{nd} order at $\theta_{\mathrm{in}} = 50°$, which shows a red shift. In this movie, the color is shift from green to orange. The movie consists of 3 quick cycles and a half slow cycle. In each cycle, the field tilt angle φ_{m} changes from 0° to 30° and back to 0° again. The tilt angle φ_{m} increases from 0° to 30° in last half slow cycle.